High resolution dynamic mapping of the *C. elegans* intestinal brush border

Aurélien Bidaud-Meynard[1], Flora Demouchy[1,†], Ophélie Nicolle[1,†], Anne Pacquelet[1,†], Shashi Kumar Suman[2], Camille Plancke[2], François Robin[2] and Grégoire Michaux[1,*]

[1]Univ Rennes, CNRS, IGDR (Institut de Génétique et Développement de Rennes) - UMR 6290, F-35000 Rennes, France

[2]Sorbonne Université, Inserm, CNRS, Institut de Biologie Paris-Seine (IBPS), Laboratoire de Biologie du développement, F-75005, Paris, France

[†]These authors contributed equally to this work

[*]lead contact gmichaux@univ-rennes1.fr

Abstract

The intestinal brush border is made of an array of microvilli that increases the membrane surface area for nutrient processing, absorption, and host defence. Studies on mammalian cultured epithelial cells uncovered some of the molecular players and physical constrains required to establish this apical specialized membrane. However, the building and maintenance of a brush border *in vivo* has not been investigated in detail yet. Here, we combined super-resolution imaging, transmission electron microscopy and genome editing in the developing nematode *C. elegans* to build a high-resolution and dynamic localization map of known and new markers of the brush border. Notably, we show that microvilli components are dynamically enriched at the apical membrane during microvilli outgrowth and maturation but become highly stable once microvilli are built. This new mapping tool will be instrumental to understand the molecular processes of microvilli growth and maintenance *in vivo* as well as the effect of genetic perturbations, notably in the context of disorders affecting brush border integrity.

Introduction

The intestinal exchange surface required for efficient nutrient absorption is reached through three consecutive morphogenic processes in mammals: elongation and folding of the intestinal tube, generation of villus protrusions and establishment of microvilli at the surface of each enterocyte, which together amplify the tube area nearly 100-times (Helander and Fandriks, 2014). Generation of microvilli in mammals occurs during enterocyte differentiation along the crypt-villus axis with the nucleation of actin filaments anchored on an F-actin- and intermediate filament-based terminal web. These core-actin bundles are then organized into a well-ordered and tightly packed array by various actin crosslinking and bundling factors, such as villin, espin and plastin1/fimbrin (Sauvanet et al., 2015). Recent studies in epithelial cell lines identified new functional players, such as IRTKS or myosin 1a/6/7b (Crawley et al., 2014a, Postema et al., 2018), and new mechanisms of brush border assembly and maintenance by vesicular trafficking (Vogel et al., 2015), microvilli motility, contraction and clustering (Meenderink et al., 2019, Chinowsky et al., 2020) or intermicrovillar protocadherin bridges (Crawley et al., 2014b). Additionally, recent use of live imaging revealed some of the key initiation and maturation steps of microvilli biogenesis in cell lines (Gaeta et al., 2021). However, a description of brush border formation and maintenance *in vivo* is lacking.

The soil nematode *C. elegans* has been widely used as a *in vivo* model of intestinal luminogenesis, polarity, and host defence (Zhang et al., 2013, Zhang and Hou, 2013, Sato et al., 2014). Intestinal organogenesis in *C. elegans* encompasses cell division and intercalation steps from the E blastomere ancestor to form a primordium containing two rows of eight cells (E16 stage) which ends up, after a last round of division, with twenty cells arranged into nine rings (or *ints*) forming a ellipse-shaped tube that runs along the whole body of the worm (Leung et al., 1999, Asan et al., 2016). Contrary to the 3-5-days living mammalian enterocytes that arise from the proliferation of crypt based columnar stem cells, the *C. elegans* intestine is

54 composed of perennial epithelial cells (Walton et al., 2016, McGhee, 2007). Their polarization
55 begins at the E16 stage and encompasses cellular components relocalization and cell shape
56 changes (Leung et al., 1999) as well as the apical accumulation of the polarity determinant
57 PAR-3 which recruits the other members of the PAR polarity complex (Feldman and Priess,
58 2012, Achilleos et al., 2010). Luminogenesis concomitantly occurs at the E16 stage with the
59 formation of apical cavities at the midline that ultimately form a lumen, a process that probably
60 involves vesicular trafficking (Leung et al., 1999). *C. elegans* enterocytes displays a brush
61 border that is structurally similar to that of mammals (Leung et al., 1999, Geisler et al., 2019,
62 Bidaud-Meynard et al., 2019) and relies on some of the same structural components. Indeed, *C.*
63 *elegans* microvilli are made of F-actin core bundles, notably the intestinal-specific isoform of
64 actin *act-5*, whose depletion induces a circular lumen with sparse and defective microvilli
65 (MacQueen et al., 2005). Several F-actin regulators have been shown to be essential for *C.*
66 *elegans* brush border integrity, such as *erm-1*, the only ortholog of the Ezrin/Radixin/Moesin
67 family (Gobel et al., 2004, Van Furden et al., 2004) and the actin capping factor EPS-8 (Croce
68 et al., 2004). As in mammals, these microvilli are anchored on a terminal web made of a network
69 of F-actin and various intermediate filament isoforms forming an electron-dense belt named as
70 endotube, in which IFB-2 plays a major role (Geisler et al., 2020, Bossinger et al., 2004). Hence,
71 the structural and biochemical similarity with mammals make *C. elegans* an appropriate model
72 to study the biogenesis of microvilli *in vivo*.

73 Most of the studies in *C. elegans* focused on early polarization steps and the formation
74 of the brush border was only studied by Transmission Electron Microscopy (TEM), which
75 provides ultrastructural data but lacks the dynamics and whole organ context. Here, we
76 combined super-resolution and quantitative live microscopy, TEM and fluorescence recovery
77 after photobleaching data to characterize the recruitment and dynamics of endogenously tagged
78 markers during the establishment of the brush border *in vivo* in *C. elegans*.

79

Results and discussion

TEM analysis of the brush border establishment in *C. elegans* developing embryo.

To first characterize the development of the brush border *in vivo*, embryos and larvae at various developmental stages were analysed by TEM (Nicolle et al., 2015). We observed that the intestinal lumen starts to open at the comma stage and progressively expands to reach the renown elliptic shape in larvae (Fig. 1A-B). At the apex, the first microvilli-like membrane extensions were observed at the 1.5-fold stage and started to cover the apical membrane, with a disorganized pattern, at the 2.5-fold stage, to finally form a regular brush border from the 3-fold stage (Fig. 1A). Measurements suggest a relatively continuous increase in microvilli density, length and width (Figs 1A-E and S1A-C) which implies a gradual maturation of the brush border as well as *de novo* growth of microvilli throughout development to fill in the membrane added during intestinal surface expansion (Fig. 1A, arrows). Finally, transversal imaging of the brush border allowed to measure the distance between microvilli edges and centres (76,0 ± 1,1 nm and 203,2 ± 2,0 nm, respectively) (Fig. 1F-G).

Dynamic recruitment of brush border components during *C. elegans* development.

Expression profiling in mammalian enterocytes between the proliferative crypt and the terminally differentiated villus demonstrated a marked upregulation of actin cytoskeleton-related genes, including actin, ezrin, villin and espin (Chang et al., 2008, Mariadason et al., 2005). Notably, recent data in LLC-PK1 cells showed a stepwise recruitment of EPS8 and IRTKS first, and then ezrin, during microvilli outgrowth (Gaeta et al., 2021). We hypothesized that a set of brush border components may specifically be recruited at the apical pole during brush border establishment *in vivo*. To test this, we performed a systematic analysis of the apical localization of endogenously tagged known brush border markers and putative new components, based on expression patterns as well as sequence or function homology with microvilli-associated mammalian proteins.

105 This led first to the identification of PLST-1, the ortholog of plastin1/fimbrin (Figs 2A
106 and S2), which is one of the major F-actin organizing factor in mammalian cells brush borders,
107 together with ezrin, villin and espin (Crawley et al., 2014a). While the ortholog of villin seems
108 not to be localized at the brush border (Hunt-Newbury et al., 2007) and espin does not have a
109 *C. elegans* ortholog, PLST-1 has been involved in cortical contractility in the *C. elegans* zygote
110 (Ding et al., 2017) but has not been studied in the intestine yet. Second, the F-actin cross-linker
111 FLN-2 (the ortholog of filamin A), that has been proposed to play a role in brush border
112 maintenance in mammalian models (Zhou et al., 2014) was also localized at the enterocytes
113 apical membrane in *C. elegans* (Figs 2B and S2).

114 In addition to these actin cytoskeleton organizing factors, many members of the myosin
115 superfamily of actin motors have been localized to the brush border in mammalian cells
116 (McConnell et al., 2011, Sauvanet et al., 2015). This superfamily comprises 12 classes of
117 conventional and unconventional myosins, which function as multimers of heavy and light
118 chains (Fili and Toseland, 2019). In the brush border, they have been shown to fulfil structural
119 (e.g. MYO7b, MYH14), trafficking (e.g. MYO-1a, -6) as well as contractile (non-muscle
120 myosin NM2C) functions (Houdusse and Titus, 2021, Chinowsky et al., 2020). We found that
121 a specific set of myosins accumulates at the enterocytes apex throughout *C. elegans*
122 development: i) the unconventional heavy chain HUM-5 (the ortholog of human MYO1d/g)
123 which is also localized at the lateral membrane (Figs 2D, S2), but not the other members of this
124 class, HUM-1 and HUM-2 (Fig S3A-B); ii) the essential myosin light chain MLC-5 (Gally et
125 al., 2009) (the ortholog of human MYL1/6) accumulated at the apical membrane of the
126 enterocytes in both embryos and larvae (Figs 2D, S2), while MLC-4 was only weakly expressed
127 in embryos (Fig S3C). Interestingly, we found that NMY-1 and NMY-2 (the orthologs of the
128 non-muscle myosins NM2A/B and NM2B/C, respectively) (Fig. S3D-E), did not, or only very
129 weakly for NMY-1, accumulate apically, which suggests that myosin-dependent contractility

130 may be less crucial for microvilli assembly in *C. elegans* than in mammals (Chinowsky et al.,
131 2020). These results suggest species-specific mechanisms or compensation between myosins,
132 as shown before (Houdusse and Titus, 2021), and the need for systematic approaches to better
133 characterize the conserved components of brush borders, for instance to identify putative
134 intermicrovillar bridges molecules (e.g. protocadherins) (Crawley et al., 2014b) among the
135 various cadherin-like proteins in the *C. elegans* genome (Loveless and Hardin, 2012).

136 To quantitatively assess the expression of these apically enriched factors during brush
137 border establishment, we used photon counting detectors and quantified the absolute apical
138 signal of endogenously tagged proteins at all *C. elegans* developmental stages (Figs 2S, S2 and
139 S3F). Notably, we observed that a set of markers was already localized at the apical PM at the
140 lima bean stage, before microvilli onset: ERM-1, FLN-2, PLST-1, ACT-5 (note that ACT-5
141 was exogenously expressed under its own promoter, because of the embryonic lethality of
142 endogenously tagged strains), as well as the intermediate filament IFB-2, which appears slightly
143 later (Figs 2E-J and S2). Then, we observed that the apical localization of these markers, as
144 well as that of the actin polymerization/severing agent EPS-8, HUM-5 and MLC-5,
145 dramatically increased concomitantly with microvilli assembly (from the 1.5-fold stage), most
146 of them peaked between the 4-fold and L1 stages and then decreased until adulthood (Fig. 2K-
147 S and S2). The early accumulation of some of these factors at the apical membrane might reflect
148 their importance for microvilli assembly, which is consistent with the requirement of ERM-1
149 and ACT-5 (Gobel et al., 2004, MacQueen et al., 2005) and the direct relationship between G-
150 actin apical availability and microvilli growth (Faust et al., 2019). As PLST-1 also accumulated
151 before microvilli onset, it could also play a role in microvilli initial assembly *in vivo*, which is
152 coherent with the disorganized terminal web and microvilli rootlets described in *Pls1* knockout
153 mice (Grimm-Gunter et al., 2009), despite no obvious defect in *plst-1 C. elegans mutants* at
154 larval stages (not shown). Interestingly, we observed that FLN-2 displayed a shifted pattern,

155 with an earlier peak that may suggest a specific role in microvilli establishment. Thus, an
156 evolving set of factors might control microvilli building in *C. elegans*: a *pre-assembly* module,
157 composed, at least, of ERM-1, ACT-5, PLST-1, FLN-2 and IFB-2 ; an *assembly module*,
158 composed additionally of EPS-8, HUM-5 and MLC-5 and, finally, a *mature module* that does
159 not require FLN-2 (Fig. S5B).

160 **Super-resolution imaging of the brush border *in vivo***

161 According to the Rayleigh criterion (Rfluo= $\frac{1.22\lambda}{2 \text{ x NA}}$), the optical axial resolution of
162 the 405, 488 and 561 nm lasers is 176.5, 212.6 and 244.4 nm, respectively, using a NA1.4
163 objective, which is at the limit to resolve individual microvilli (~100 nm between edges, ~200
164 nm between centers, ~120 nm wide, Fig. 1E, G). To test this, we inserted three different tags at
165 the C-terminal end of the brush border-specific factor ERM-1 by CRISPR-CAS9: Blue
166 Fluorescent Protein (mTagBFP2/BFP, λ_{Ex} 381 nm/λ_{Em} 445 nm) (Subach et al., 2011),
167 mNeongreen (mNG, λ_{Ex} 506 nm/λ_{Em} 517 nm) (Shaner et al., 2013) and wrmScarlet (wSc, λ_{Ex}
168 569 nm/λ_{Em} 593 nm) (El Mouridi et al., 2017) and imaged them with a multi-detector and
169 deconvolution-based super-resolution imaging system (see methods). We could easily visualize
170 the regular alignment of microvilli with BFP and mNG tags, but it was less visible with the wSc
171 fluorophore (Fig. 3A-B). In addition to individual microvilli, we could also precisely localize
172 brush border markers along the microvilli long axis. Indeed, while ERM-1 covered the whole
173 microvilli length, the chloride intracellular channel 2 (CLIC-2) ortholog EXL-1 (Liang et al.,
174 2017) accumulated at the tip of microvilli (Fig. 3C) and the P-GlycoProtein related transporter
175 PGP-1 at their base (Bidaud-Meynard et al., 2019). Of note, this method allowed to uncover
176 localization differences between in-locus mNG-tagged and overexpressed GFP-tagged proteins
177 (compare Figs 3C and S4A), as already reported for E-cadherin in the same tissue (Cordova-
178 Burgos et al., 2021). Individual microvilli were similarly visualized using Random Illumination
179 Microscopy (Mangeat et al., 2021), but not using conventional confocal or Stimulated-

180 emission-depletion (STED) microscopes, probably because of the depth of the intestine inside
181 the nematode body (~15µm) (Fig S4B). The brush border could also be imaged transversally
182 (compare Figs 3D and 1F). Hence, the combination of a specific super-resolution imaging
183 system, appropriate fluorophores and endogenous expression allows the precise visualization
184 of microvilli *in vivo* in *C. elegans* intestine.

185 We then used these tools to study the (co)localization of known and newly identified
186 apical markers in adult worms, as we have done before for ERM-1 and ACT-5 (Bidaud-
187 Meynard et al., 2019). Using a strain co-expressing endogenously tagged versions of the three
188 classical microvilli markers ERM-1, EPS-8, and IFB-2, we observed that ERM-1 localized
189 along the whole microvilli but not in the terminal web (Fig. 3E). EPS-8 accumulated at the tip
190 of the microvilli, where it partially colocalized with ERM-1, and was also found marginally at
191 the terminal web vicinity, as observed before by immuno-EM (Croce et al., 2004) (Fig. 3E).
192 Finally, we could resolve in some worms the tiny difference between ACT-5, which localized
193 along and at the basis of the microvilli, and the endotube marker IFB-2 (Geisler et al., 2019,
194 Bossinger et al., 2004), with which it composes the terminal web (Fig. S4C).

195 Notably, we found that PLST-1 localized at the bottom of the microvilli (Fig. 3F), with
196 a doted pattern different from the linear terminal web pattern (IFB-2 in Fig 3E). This
197 localization is consistent with that of Plastin-1 in mouse jejunum sections and its proposed role
198 in anchoring microvillar actin rootlets to the terminal web (Grimm-Gunter et al., 2009). While
199 FLN-2 was hardly detectable in adult worms, we observed in L1 larvae that FLN-2 localized at
200 the basis of microvilli (Fig. 3G), alike MLC-5, which also partly decorated the whole microvilli
201 (Fig. 3H). Finally, we found that HUM-5 accumulates at both the basis and the tip of, and
202 localizes slightly along microvilli (Fig. 3I), a similar pattern to that described in mouse intestine
203 (Benesh et al., 2010). Thus, our novel approach allowed to visualize *in vivo* the expression and

204 the precise localization of several proteins of the brush border including structural proteins and
205 molecular motors.

206 Since factors needed to build the microvilli are concomitantly recruited to the apical
207 pole (Fig. 2), we finally asked whether super-resolution imaging could resolve the change in
208 their relative microvillar position during brush border assembly. Line scans showed that ERM-
209 1, EPS-8 and IFB-2 colocalized at the beginning of microvilli assembly (2-fold stage) and
210 progressively moved away to end up with IFB-2 and EPS-8 contralaterally positioned and
211 surrounding ERM-1 (Figs 3J-K and S4D).

212 **Analysis of brush border markers dynamics during microvilli assembly**

213 To test whether the progressive accumulation of brush border components at the apical
214 membrane implies a dynamic behaviour during microvilli building (Fig. 2S), we analysed the
215 dynamics of ERM-1 during and after the establishment of the brush border using *fluorescence*
216 *recovery after photobleaching* (FRAP) experiments. While ERM-1 was very dynamic during
217 microvilli assembly (1.5-fold embryo) it became surprisingly extremely stable in established
218 brush border (adult worm), with little recovery even after >15 minutes (Figs 4A and S5A),
219 confirming recent observations (Ramalho et al., 2020, Remmelzwaal et al., 2021). Systematic
220 analysis of ERM-1 fluorescence recovery throughout *C. elegans* development confirmed that
221 ERM-1 dynamics progressively decreased concomitantly with brush border assembly and
222 became almost static in larvae and adults (Fig. 4B, F-G). To confirm this, the dynamics of other
223 structural components of the brush border was analysed during microvilli initial assembly
224 (Comma/1.5-fold), maturation (L1 larvae) and in adult worms; note that due to embryo fast
225 movements from the 2-fold stage to the end of embryogenesis, these developmental stages
226 could not be investigated. Like ERM-1, EPS-8 was also very dynamic during microvilli
227 assembly but became highly stable in maturating and mature microvilli (Fig. 4C, F-G). ACT-5
228 also displayed a dynamic, albeit of a lower extend, behaviour, that persisted until L1 larvae

229 (Fig. 3D, F-G), in agreement with F-actin mobile fractions in Caco-2 cells (~60%) (Waharte et
230 al., 2005), to finally become stable at adulthood. Conversely, the intermediate filament IFB-2
231 displayed a more stable behaviour at every developmental stage, which reflects its anchoring
232 role for growing microvilli (Grimm-Gunter et al., 2009, Geisler et al., 2019).

233 Thus, these results enlightened that mature microvilli adopt a stable steady state *in vivo,*
234 which is consistent with the notion that microvilli might be considered more as stereocilia than
235 evanescent F-actin-based structures like filopodia. The maturation status of the brush border
236 might be a key consideration that would help to reconcile conflicting data of the literature.
237 Indeed, probably immature microvilli in non-polarized cells seem to be more dynamic, i.e. life-
238 cycle of ~12 min in A6 cells (Gorelik et al., 2003), with an intense actin treadmilling (half-time
239 recovery of ezrin of ~30 s) (Garbett and Bretscher, 2012) but which were found to last up to 12
240 h in mature brush borders (Meenderink et al., 2019). This high stability could contribute to
241 explain their uniform length and highly ordered organisation in the human intestine (Crawley
242 et al., 2014a).

243 In conclusion, this new multi-imaging approach allowed to image the precise
244 localization of brush border markers at the microvilli level *in vivo* and to study the dynamic
245 recruitment of microvilli components during the development of the brush border. This new
246 methodology will be instrumental to address the many questions remaining to understand
247 microvilli assembly and maturation, notably on the full set of factors required for microvilli
248 growth and maintenance, the principles that govern microvilli size, packing and organization
249 or the motility of microvilli *in vivo*. It will be also essential to understand the pathophysiology
250 of diseases affecting the brush border, such as Microvillus inclusions disease (Bidaud-Meynard
251 et al., 2019), Crohn's (VanDussen et al., 2018) and celiac (Tye-Din and Anderson, 2008)
252 diseases, or pathogen infections (Scott et al., 2004, Lauwaet et al., 2004), as well as intestinal
253 aging.

254 # Materials and methods

255 ## *C. elegans* strains and maintenance

256 Strains were maintained under typical conditions as described (Brenner, 1974). CRISPR-
257 CAS9-genome edited mTagBFP2, mNeonGreen and mScarlet-tagged proteins were generated
258 at the « Biologie de *Cænorhabditis elegans* » facility (Universite Lyon 1, UMS3421, Lyon,
259 France). The strains used in this study are listed in Table S1.

260 ## *in vivo* confocal imaging in *C. elegans*

261 For *in vivo* imaging, *C. elegans* larvae were mounted on a 10% agarose pad in a solution of 100
262 nm polystyrene microbeads (Polysciences Inc.) to stop worm movement. Embryos were
263 mounted on a 2% agarose pad with a mix of bacteria and M9 medium (localization) or M9 only
264 (live imaging). Single confocal slices of the anterior intestinal cells or stacks of the whole
265 intestine were performed on adults/larvae and whole embryos, respectively, using a Leica SP8
266 (Wetzlar, Germany) equipped with a 63X, 1.4 NA objective (LAS AF software) or a super-
267 resolution Zeiss LSM880-Airyscan (Oberkochen, Germany) equipped with a 63X, 1.4 NA
268 objective (Zen Black software). Quantitative recording of the apical localization of brush border
269 markers was performed on the Leica SP8 microscope using the photon counting function of
270 HyD hybrid detectors and image accumulation (Fig. S3). For embryos, stacks were
271 reconstructed using the max intensity Z-projection function of Fiji software
272 (https://imagej.net/Fiji). All images were examined using Fiji software.

273 ## TEM

274 Samples were subjected to high-pressure freezing followed by freeze substitution, flat
275 embedding, targeting, and sectioning using the positional correlation and tight trimming
276 approach, as described previously (Bidaud-Meynard et al., 2019). Each embryo or larva was
277 sectioned in 5-10 different places, every 5-7 µm, to ensure that different intestinal cells were
278 observed. Ultrathin sections (60-70 nm) were collected on formvar-coated slot grids (FCF2010-

279 CU, EMS) and observed using a JEM-1400 transmission electron microscope (JEOL, Tokyo,
280 Japan) operated at 120 kV, equipped with a Gatan Orius SC 1000 camera (Gatan, Pleasanton,
281 USA) and piloted by the Digital Micrograph program.

282 **Fluorescence recovery after photobleaching (FRAP)**

283 FRAP experiments were performed using the Zeiss LSM880-Airyscan on a rectangle ROI of
284 1,3 µm width crossing the apical PM with 100% 488 nm laser power, 10-20 iterations and
285 recovery was measured every 30 s for 10 to 15 min. Post-FRAP images were analysed using
286 the Fiji software. The mean fluorescence intensity of the bleached ROI was normalized for
287 photobleaching by recording the intensity of the same ROI on a non-bleached region and
288 cytoplasmic background was subtracted on each frame. Finally, the % recovery was calculated
289 on each timeframe by comparing the normalized signal intensities with the mean of two
290 timepoints before bleach. Curve fitting was performed with one-phase association non-linear
291 regression analysis using Graphpad Prism 9 software. The mobile fraction (Mf) was calculated
292 with the following equation: $Mf = \frac{I\infty - I0}{Ii - I0}$, where I_∞ is the signal intensity at the endpoint plateau
293 phase, I_i is the mean of two pre-bleached signal intensities and I_0 is the signal intensity at the
294 first post-bleach timepoint.

295 **Quantification**

296 Micrographs were analysed using Fiji software and were representative of all the
297 sections observed. Microvilli (length, width, density) and lumen perimeter were quantified on
298 at least 6-13 TEM images per sample (n≥3, by developmental stage).

299 For the quantitative measurement of the apical localization of brush border markers, a
300 maximum intensity projection was performed using Fiji, and the signal density was quantified
301 by measuring the mean fluorescence signal along a segmented line covering the whole intestine
302 (E16 to 2-fold embryos) or visible part of the anterior intestine (3-fold to adults). The signal
303 measured was then corrected for fluorescence accumulation and normalized.

304 **Statistical analysis**

305 Results are presented as mean ± SEM of the number of independent experiments
306 indicated in the legends, and scattered dots represent individual worms. p-values were
307 calculated by two-tailed unpaired student's t-test or one-way ANOVA, as indicated in the figure
308 captions, and a 95% confidence level was considered significant. Normal distribution of data
309 and homogeneity of variances were validated using the Shapiro-Wilk and the Bartlett (for
310 ANOVA) or F (for student) tests, respectively. Mann-Whitney or Kruskal-Wallis tests were
311 used for calculating the P-values between two or multiple non-normal distributions,
312 respectively, and Dunnett's tests was used for multiple distributions with non-homogenous
313 variances.

Acknowledgements

We thank Marc Tramier and Stéphanie Dutertre for their advice on fluorescence quantification and super-resolution imaging, respectively, as well as Matis Soleilhac for the initial analysis of expression patterns. We also thank Michel Labouesse, Junho Lee and Ronen Zaidel-Bar for strains as well as Céline Burcklé and Guillaume Halet for helpful discussions. Some strains were provided by the CGC, which is funded by NIH Office of research Infrastructure Programs (P40 OD010440; University of Minnesota, USA). We are grateful to Maité Carre-Pierrat who performed CRISPR-CAS9 endogenous tagging at the Biology of *Caenorhabditis elegans* Facility, Universite Lyon 1, UMS3421, France. Photonic and electron microscopy imaging were performed at the Microscopy Rennes imaging Center (MRiC, Biosit, Rennes, France), member of the national infrastructure France-BioImaging supported by the French National Research Agency (ANR-10-INBS-04).

Funding

This work was supported by the European Union's Horizon 2020 research and innovation program under the Marie Sklodowska-Curie grant agreement 844070 to ABM, Défis scientifiques de l'Université Rennes 1 (17CQ436-S0) to ABM and GM, Ligue Régionale Contre le Cancer (22, 29, 35, 41, 72, 85) and the Fondation maladies rares (169608 and EXM-2019-1013) to GM. GM laboratory also received institutional funding from the CNRS and the Université de Rennes 1.

Authors contribution

Conceptualization: A.B.M., G.M.; Methodology, Validation, Formal analysis, Investigation, Data curation: A.B.M., F.D., O.N., A.P., G.M.; Ressources: S.K.S., C.P., F.R.; Writing - original draft: A.B.M. G.M.; Writing - review & editing: A.B.M., O.N., A.P., G.M.; Supervision: G.M; Funding acquisition: A.B.M., G.M.

Conflict of interest

The authors declare no conflict of interest.

340 # References

341 ACHILLEOS, A., WEHMAN, A. M. & NANCE, J. 2010. PAR-3 mediates the initial clustering and apical
342 localization of junction and polarity proteins during C. elegans intestinal epithelial cell
343 polarization. *Development,* 137**,** 1833-42.

344 ASAN, A., RAIDERS, S. A. & PRIESS, J. R. 2016. Morphogenesis of the C. elegans Intestine Involves
345 Axon Guidance Genes. *PLoS Genet,* 12**,** e1005950.

346 BENESH, A. E., NAMBIAR, R., MCCONNELL, R. E., MAO, S., TABB, D. L. & TYSKA, M. J. 2010. Differential
347 localization and dynamics of class I myosins in the enterocyte microvillus. *Mol Biol Cell,* 21**,**
348 970-8.

349 BIDAUD-MEYNARD, A., NICOLLE, O., HECK, M., LE CUNFF, Y. & MICHAUX, G. 2019. A V0-ATPase-
350 dependent apical trafficking pathway maintains the polarity of the intestinal absorptive
351 membrane. *Development,* 146.

352 BOSSINGER, O., FUKUSHIGE, T., CLAEYS, M., BORGONIE, G. & MCGHEE, J. D. 2004. The apical
353 disposition of the Caenorhabditis elegans intestinal terminal web is maintained by LET-413.
354 *Dev Biol,* 268**,** 448-56.

355 BRENNER, S. 1974. The genetics of Caenorhabditis elegans. *Genetics,* 77**,** 71-94.

356 CHANG, J., CHANCE, M. R., NICHOLAS, C., AHMED, N., GUILMEAU, S., FLANDEZ, M., WANG, D., BYUN,
357 D. S., NASSER, S., ALBANESE, J. M., CORNER, G. A., HEERDT, B. G., WILSON, A. J.,
358 AUGENLICHT, L. H. & MARIADASON, J. M. 2008. Proteomic changes during intestinal cell
359 maturation in vivo. *J Proteomics,* 71**,** 530-46.

360 CHINOWSKY, C. R., PINETTE, J. A., MEENDERINK, L. M., LAU, K. S. & TYSKA, M. J. 2020. Nonmuscle
361 myosin-2 contractility-dependent actin turnover limits the length of epithelial microvilli. *Mol*
362 *Biol Cell,* 31**,** 2803-2815.

363 CORDOVA-BURGOS, L., PATEL, F. B. & SOTO, M. C. 2021. E-Cadherin/HMR-1 Membrane Enrichment
364 Is Polarized by WAVE-Dependent Branched Actin. *J Dev Biol,* 9.

365 CRAWLEY, S. W., MOOSEKER, M. S. & TYSKA, M. J. 2014a. Shaping the intestinal brush border. *J Cell*
366 *Biol,* 207**,** 441-51.

367 CRAWLEY, S. W., SHIFRIN, D. A., JR., GREGA-LARSON, N. E., MCCONNELL, R. E., BENESH, A. E., MAO,
368 S., ZHENG, Y., ZHENG, Q. Y., NAM, K. T., MILLIS, B. A., KACHAR, B. & TYSKA, M. J. 2014b.
369 Intestinal brush border assembly driven by protocadherin-based intermicrovillar adhesion.
370 *Cell,* 157**,** 433-446.

371 CROCE, A., CASSATA, G., DISANZA, A., GAGLIANI, M. C., TACCHETTI, C., MALABARBA, M. G., CARLIER,
372 M. F., SCITA, G., BAUMEISTER, R. & DI FIORE, P. P. 2004. A novel actin barbed-end-capping
373 activity in EPS-8 regulates apical morphogenesis in intestinal cells of Caenorhabditis elegans.
374 *Nat Cell Biol,* 6**,** 1173-9.

375 DING, W. Y., ONG, H. T., HARA, Y., WONGSANTICHON, J., TOYAMA, Y., ROBINSON, R. C., NEDELEC, F.
376 & ZAIDEL-BAR, R. 2017. Plastin increases cortical connectivity to facilitate robust polarization
377 and timely cytokinesis. *J Cell Biol,* 216**,** 1371-1386.

378 EL MOURIDI, S., LECROISEY, C., TARDY, P., MERCIER, M., LECLERCQ-BLONDEL, A., ZARIOHI, N. &
379 BOULIN, T. 2017. Reliable CRISPR/Cas9 Genome Engineering in Caenorhabditis elegans Using
380 a Single Efficient sgRNA and an Easily Recognizable Phenotype. *G3 (Bethesda),* 7**,** 1429-1437.

381 FAUST, J. J., MILLIS, B. A. & TYSKA, M. J. 2019. Profilin-Mediated Actin Allocation Regulates the
382 Growth of Epithelial Microvilli. *Curr Biol,* 29**,** 3457-3465 e3.

383 FELDMAN, J. L. & PRIESS, J. R. 2012. A role for the centrosome and PAR-3 in the hand-off of MTOC
384 function during epithelial polarization. *Curr Biol,* 22**,** 575-82.

385 FILI, N. & TOSELAND, C. P. 2019. Unconventional Myosins: How Regulation Meets Function. *Int J Mol*
386 *Sci,* 21.

387 GAETA, I. M., MEENDERINK, L. M., POSTEMA, M. M., CENCER, C. S. & TYSKA, M. J. 2021. Direct
388 visualization of epithelial microvilli biogenesis. *Curr Biol*.

389 GALLY, C., WISSLER, F., ZAHREDDINE, H., QUINTIN, S., LANDMANN, F. & LABOUESSE, M. 2009. Myosin
390 II regulation during C. elegans embryonic elongation: LET-502/ROCK, MRCK-1 and PAK-1,
391 three kinases with different roles. *Development,* 136**,** 3109-19.

392 GARBETT, D. & BRETSCHER, A. 2012. PDZ interactions regulate rapid turnover of the scaffolding
393 protein EBP50 in microvilli. *J Cell Biol,* 198**,** 195-203.

394 GEISLER, F., COCH, R. A., RICHARDSON, C., GOLDBERG, M., BEVILACQUA, C., PREVEDEL, R. & LEUBE,
395 R. E. 2020. Intestinal intermediate filament polypeptides in C. elegans: Common and isotype-
396 specific contributions to intestinal ultrastructure and function. *Sci Rep,* 10**,** 3142.

397 GEISLER, F., COCH, R. A., RICHARDSON, C., GOLDBERG, M., DENECKE, B., BOSSINGER, O. & LEUBE, R.
398 E. 2019. The intestinal intermediate filament network responds to and protects against
399 microbial insults and toxins. *Development,* 146.

400 GOBEL, V., BARRETT, P. L., HALL, D. H. & FLEMING, J. T. 2004. Lumen morphogenesis in C. elegans
401 requires the membrane-cytoskeleton linker erm-1. *Dev Cell,* 6**,** 865-73.

402 GORELIK, J., SHEVCHUK, A. I., FROLENKOV, G. I., DIAKONOV, I. A., LAB, M. J., KROS, C. J.,
403 RICHARDSON, G. P., VODYANOY, I., EDWARDS, C. R., KLENERMAN, D. & KORCHEV, Y. E. 2003.
404 Dynamic assembly of surface structures in living cells. *Proc Natl Acad Sci U S A,* 100**,** 5819-22.

405 GRIMM-GUNTER, E. M., REVENU, C., RAMOS, S., HURBAIN, I., SMYTH, N., FERRARY, E., LOUVARD, D.,
406 ROBINE, S. & RIVERO, F. 2009. Plastin 1 binds to keratin and is required for terminal web
407 assembly in the intestinal epithelium. *Mol Biol Cell,* 20**,** 2549-62.

408 HELANDER, H. F. & FANDRIKS, L. 2014. Surface area of the digestive tract - revisited. *Scand J*
409 *Gastroenterol,* 49**,** 681-9.

410 HOUDUSSE, A. & TITUS, M. A. 2021. The many roles of myosins in filopodia, microvilli and stereocilia.
411 *Curr Biol,* 31**,** R586-R602.

412 HUNT-NEWBURY, R., VIVEIROS, R., JOHNSEN, R., MAH, A., ANASTAS, D., FANG, L., HALFNIGHT, E.,
413 LEE, D., LIN, J., LORCH, A., MCKAY, S., OKADA, H. M., PAN, J., SCHULZ, A. K., TU, D., WONG, K.,
414 ZHAO, Z., ALEXEYENKO, A., BURGLIN, T., SONNHAMMER, E., SCHNABEL, R., JONES, S. J.,
415 MARRA, M. A., BAILLIE, D. L. & MOERMAN, D. G. 2007. High-throughput in vivo analysis of
416 gene expression in Caenorhabditis elegans. *PLoS Biol,* 5**,** e237.

417 LAUWAET, T., OLIVEIRA, M. J., CALLEWAERT, B., DE BRUYNE, G., MAREEL, M. & LEROY, A. 2004.
418 Proteinase inhibitors TPCK and TLCK prevent Entamoeba histolytica induced disturbance of
419 tight junctions and microvilli in enteric cell layers in vitro. *Int J Parasitol,* 34**,** 785-94.

420 LEUNG, B., HERMANN, G. J. & PRIESS, J. R. 1999. Organogenesis of the Caenorhabditis elegans
421 intestine. *Dev Biol,* 216**,** 114-34.

422 LIANG, J., SHAULOV, Y., SAVAGE-DUNN, C., BOISSINOT, S. & HOQUE, T. 2017. Chloride intracellular
423 channel proteins respond to heat stress in Caenorhabditis elegans. *PLoS One,* 12**,** e0184308.

424 LOVELESS, T. & HARDIN, J. 2012. Cadherin complexity: recent insights into cadherin superfamily
425 function in C. elegans. *Curr Opin Cell Biol,* 24**,** 695-701.

426 MACQUEEN, A. J., BAGGETT, J. J., PERUMOV, N., BAUER, R. A., JANUSZEWSKI, T., SCHRIEFER, L. &
427 WADDLE, J. A. 2005. ACT-5 is an essential Caenorhabditis elegans actin required for intestinal
428 microvilli formation. *Mol Biol Cell,* 16**,** 3247-59.

429 MANGEAT, T., LABOUESSE, S., ALLAIN, M., NEGASH, A., MARTIN, E., GUÉNOLÉ, A., POINCLOUX, R.,
430 ESTIBAL, C., BOUISSOU, A., CANTALOUBE, S., VEGA, E., LI, T., TROUVIÈRE, C., ALLART, S.,
431 KELLER, D., DEBARNOT, V., WANG, X. B., MICHAUX, G., PINOT, M., LE BORGNE, R., TOURNIER,
432 S., SUZANNE, M., IDIER, J. & SENTENAC, A. 2021. Super-resolved live-cell imaging using
433 random illumination microscopy. *Cell Reports Methods,* 1.

434 MARIADASON, J. M., NICHOLAS, C., L'ITALIEN, K. E., ZHUANG, M., SMARTT, H. J., HEERDT, B. G.,
435 YANG, W., CORNER, G. A., WILSON, A. J., KLAMPFER, L., ARANGO, D. & AUGENLICHT, L. H.
436 2005. Gene expression profiling of intestinal epithelial cell maturation along the crypt-villus
437 axis. *Gastroenterology,* 128**,** 1081-8.

438 MCCONNELL, R. E., BENESH, A. E., MAO, S., TABB, D. L. & TYSKA, M. J. 2011. Proteomic analysis of the
439 enterocyte brush border. *Am J Physiol Gastrointest Liver Physiol,* 300**,** G914-26.

440 MCGHEE, J. D. 2007. The C. elegans intestine. *WormBook***,** 1-36.

441 MEENDERINK, L. M., GAETA, I. M., POSTEMA, M. M., CENCER, C. S., CHINOWSKY, C. R., KRYSTOFIAK,
442 E. S., MILLIS, B. A. & TYSKA, M. J. 2019. Actin Dynamics Drive Microvillar Motility and
443 Clustering during Brush Border Assembly. *Dev Cell,* 50**,** 545-556 e4.

444 NICOLLE, O., BUREL, A., GRIFFITHS, G., MICHAUX, G. & KOLOTUEV, I. 2015. Adaptation of Cryo-
445 Sectioning for IEM Labeling of Asymmetric Samples: A Study Using Caenorhabditis elegans.
446 *Traffic,* 16**,** 893-905.

447 POSTEMA, M. M., GREGA-LARSON, N. E., NEININGER, A. C. & TYSKA, M. J. 2018. IRTKS (BAIAP2L1)
448 Elongates Epithelial Microvilli Using EPS8-Dependent and Independent Mechanisms. *Curr*
449 *Biol,* 28**,** 2876-2888 e4.

450 RAMALHO, J. J., SEPERS, J. J., NICOLLE, O., SCHMIDT, R., CRAVO, J., MICHAUX, G. & BOXEM, M. 2020.
451 C-terminal phosphorylation modulates ERM-1 localization and dynamics to control cortical
452 actin organization and support lumen formation during Caenorhabditis elegans
453 development. *Development,* 147.

454 REMMELZWAAL, S., GEISLER, F., STUCCHI, R., VAN DER HORST, S., PASOLLI, M., KROLL, J. R.,
455 JAROSINSKA, O. D., AKHMANOVA, A., RICHARDSON, C. A., ALTELAAR, M., LEUBE, R. E.,
456 RAMALHO, J. J. & BOXEM, M. 2021. BBLN-1 is essential for intermediate filament
457 organization and apical membrane morphology. *Curr Biol*.

458 SATO, K., NORRIS, A., SATO, M. & GRANT, B. D. 2014. C. elegans as a model for membrane traffic.
459 *WormBook***,** 1-47.

460 SAUVANET, C., WAYT, J., PELASEYED, T. & BRETSCHER, A. 2015. Structure, regulation, and functional
461 diversity of microvilli on the apical domain of epithelial cells. *Annu Rev Cell Dev Biol,* 31**,** 593-
462 621.

463 SCOTT, K. G., YU, L. C. & BURET, A. G. 2004. Role of CD8+ and CD4+ T lymphocytes in jejunal mucosal
464 injury during murine giardiasis. *Infect Immun,* 72**,** 3536-42.

465 SHANER, N. C., LAMBERT, G. G., CHAMMAS, A., NI, Y., CRANFILL, P. J., BAIRD, M. A., SELL, B. R.,
466 ALLEN, J. R., DAY, R. N., ISRAELSSON, M., DAVIDSON, M. W. & WANG, J. 2013. A bright
467 monomeric green fluorescent protein derived from Branchiostoma lanceolatum. *Nat*
468 *Methods,* 10**,** 407-9.

469 SUBACH, O. M., CRANFILL, P. J., DAVIDSON, M. W. & VERKHUSHA, V. V. 2011. An enhanced
470 monomeric blue fluorescent protein with the high chemical stability of the chromophore.
471 *PLoS One,* 6**,** e28674.

472 TYE-DIN, J. & ANDERSON, R. 2008. Immunopathogenesis of celiac disease. *Curr Gastroenterol Rep,*
473 10**,** 458-65.

474 VAN FURDEN, D., JOHNSON, K., SEGBERT, C. & BOSSINGER, O. 2004. The C. elegans ezrin-radixin-
475 moesin protein ERM-1 is necessary for apical junction remodelling and tubulogenesis in the
476 intestine. *Dev Biol,* 272**,** 262-76.

477 VANDUSSEN, K. L., STOJMIROVIC, A., LI, K., LIU, T. C., KIMES, P. K., MUEGGE, B. D., SIMPSON, K. F.,
478 CIORBA, M. A., PERRIGOUE, J. G., FRIEDMAN, J. R., TOWNE, J. E., HEAD, R. D. &
479 STAPPENBECK, T. S. 2018. Abnormal Small Intestinal Epithelial Microvilli in Patients With
480 Crohn's Disease. *Gastroenterology,* 155**,** 815-828.

481 VOGEL, G. F., KLEE, K. M., JANECKE, A. R., MULLER, T., HESS, M. W. & HUBER, L. A. 2015. Cargo-
482 selective apical exocytosis in epithelial cells is conducted by Myo5B, Slp4a, Vamp7, and
483 Syntaxin 3. *J Cell Biol,* 211**,** 587-604.

484 WAHARTE, F., BROWN, C. M., COSCOY, S., COUDRIER, E. & AMBLARD, F. 2005. A two-photon FRAP
485 analysis of the cytoskeleton dynamics in the microvilli of intestinal cells. *Biophys J,* 88**,** 1467-
486 78.

487 WALTON, K. D., FREDDO, A. M., WANG, S. & GUMUCIO, D. L. 2016. Generation of intestinal surface:
488 an absorbing tale. *Development,* 143**,** 2261-72.

489 ZHANG, H., KIM, A., ABRAHAM, N., KHAN, L. A. & GOBEL, V. 2013. Vesicular sorting controls the
490 polarity of expanding membranes in the C. elegans intestine. *Worm,* 2**,** e23702.

491 ZHANG, R. & HOU, A. 2013. Host-Microbe Interactions in Caenorhabditis elegans. *ISRN Microbiol,*
492 2013**,** 356451.

493 ZHOU, X., MASSOL, R. H., NAKAMURA, F., CHEN, X., GEWURZ, B. E., DAVIS, B. M., LENCER, W. I. &
494 WALDOR, M. K. 2014. Remodeling of the intestinal brush border underlies adhesion and
495 virulence of an enteric pathogen. *mBio,* 5.

496

497

498 # Figure legends

499 **Figure 1. TEM analysis of the brush border.**

500 (A) Representative TEM images of the intestinal lumen at the *C. elegans* developmental stages
501 indicated.

502 (B-E) Quantification of the lumen perimeter (B) and microvilli density (C), length (D), and
503 width (E) from TEM images. Histograms show the mean ± SEM of the average of 3-13 slices
504 (B), 3-13 lumen (C) and 6-29 microvilli (D-E) per sample from 3-5 worms at each
505 developmental stage. Arrowheads, nascent microvilli; arrows, empty spaces between
506 microvilli; YA, young adults. n.s., non-significant, * p<0,05, **p<0,01, ***p<0,001, unpaired
507 t-test.

508 (F-G) Transversal view of the brush border in adult worms.

509 (G) The distance between microvilli edges and centres was calculated on 200 microvilli from
510 (F).

511 **Figure 2. Brush border components are dynamically enriched at the apical membrane**
512 **during microvilli assembly.**

513 (A-I) Representative images of the apical localization of GFP-tagged MLC-5, PLST-1 and
514 ACT-5, mNG-tagged ERM-1, IFB-2 and HUM-5, and mVenus-tagged FLN-2 in L1 larvae (A-
515 D) and lima bean embryos (E-I).

516 (J) The absolute apical signal of the indicated markers was measured on at least 10 embryos at
517 each developmental stage. The heatmap shows a focus on early brush border assembly steps
518 where the maximum intensity was set at the 2-fold-stage.

519 (K-R) Apical localization of the indicated markers at the 2-fold stage.

520 (S) The absolute apical localization of the indicated markers was recorded as in (J) and
521 normalized to the maximum expression for each marker. Data are mean ± SEM.

522 In all images, arrowheads show the apical plasma membrane of the intestinal cells. Scale bar, 5
523 μm.

524 **Figure 3. Super-resolution imaging of the brush border.**

525 (A-B) Super-resolution images of ERM-1 endogenously tagged with BFP, mNG and wSc in *C.*
526 *elegans* young adults. (B) represents the normalized intensity profile along a 4 µm-long dashed
527 line, as represented in (A).

528 (C) Super-resolution images of ERM-1::mNG or EXL-1::mNG in young adults.

529 (D) Transversal super-resolution image of the brush border performed on a young adult *C.*
530 *elegans* strain endogenously expressing ERM-1::mNG. The red hexagon indicates the putative
531 hexagonal packing of microvilli.

532 (E-I) Representative super-resolution images of the indicated microvilli markers endogenously
533 tagged with mNG (ERM-1, HUM-5,), GFP (PLST-1, MLC-5), BFP (EPS-8), mVenus (FLN-
534 2) or wSc (IFB-2) in young adults. Insert, higher magnification of the ROI depicted by the
535 dotted line. Closed and open arrowheads show the colocalization between ERM-1 and the
536 indicated markers at the base and along the microvilli, respectively.

537 (J-K) Left TEM images show the shape of the brush border at the corresponding developmental
538 stage. Right: super-resolution images of the brush border in 2-fold embryo and L2 larvae co-
539 expressing EPS-8::BFP, ERM-1::mNG and IFB-2::wSc. Right histograms correspond to the
540 signal intensity profile of the three markers along the line depicted on the pictures.

541 **Figure 4. Brush border components dynamics during microvilli assembly.**

542 (A-B) ERM-1::mNG was bleached in a 1.5-fold embryo and an adult worm, and fluorescence
543 recovery was observed every 30 s.

544 (B-E) Quantification of the signal recovery after bleaching of ERM-1::mNG (B), EPS-8::mNG
545 (C), ACT-5::GFP (D) and IFB-2::mNG (E), measured every 30 s on 5-11 worms at the indicated
546 developmental stages. Thin lines represent the mean ± SEM of signal recovery, bold lines
547 represent one-phase association non-linear regression fitting curves.

548 (F-G) Analysis of the FRAP experiments performed in (D-E) at the comma, 1.5-fold, L1 larva
549 and adult stages. (F) Shows the % of the pre-bleached signal (mean of two timepoints)
550 recovered at the endpoint (540 sec) and (G) shows the mobile fraction. Histograms show the
551 mean ± SEM, dots in (F) represent individual worms. The difference between variance was
552 calculated using ANOVA, *p<0,05, **p<0,01, ***p<0.001.

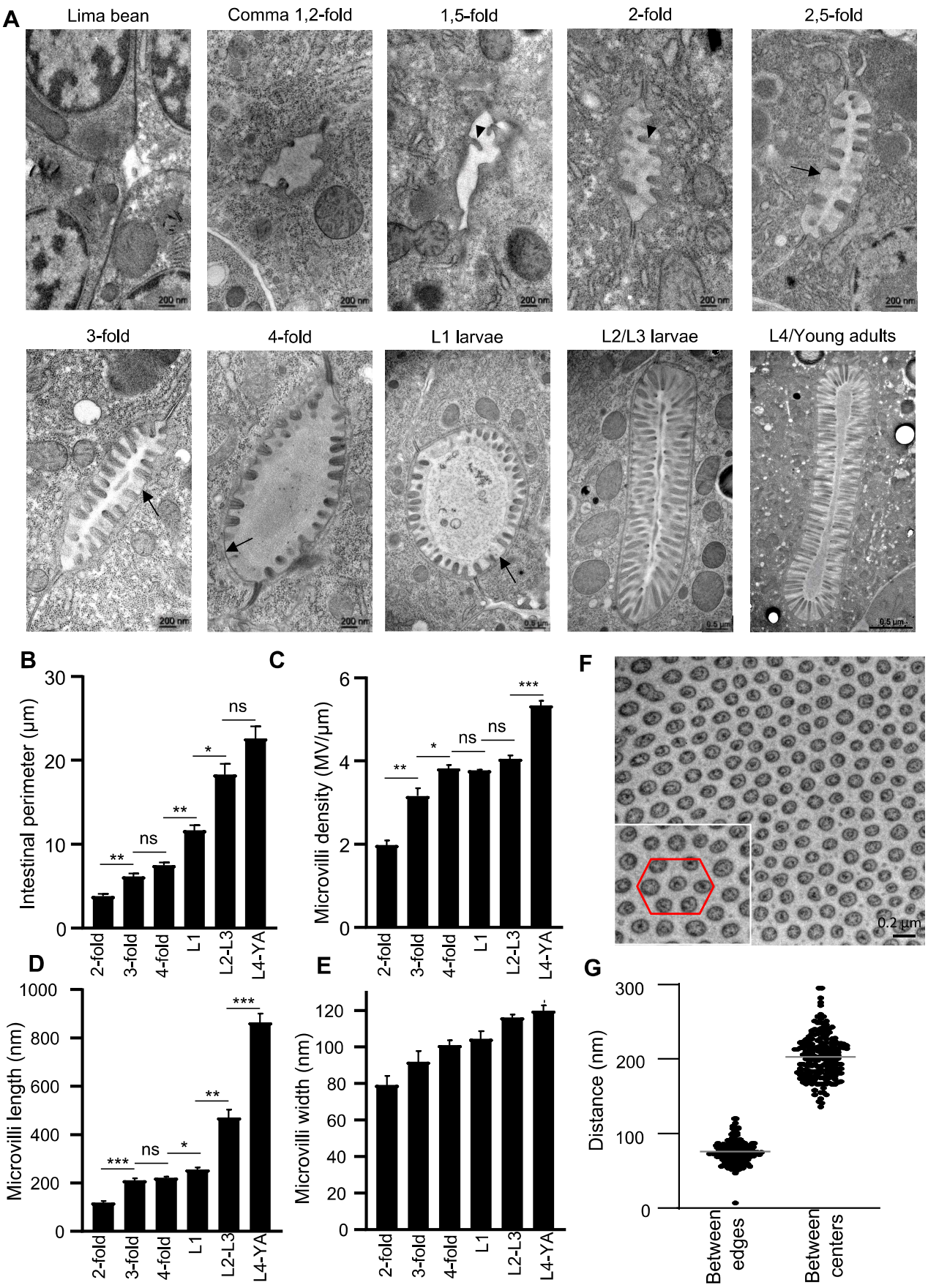
A
Lima bean
Comma 1,2-fold
1,5-fold
2-fold
2,5-fold
3-fold
4-fold
L1 larvae
L2/L3 larvae
L4/Young adults
200 nm
0.5 µm
B
Intestinal perimeter (µm)
C
Microvilli density (MV/µm)
D
Microvilli length (nm)
E
Microvilli width (nm)
2-fold
3-fold
4-fold
L1
L2-L3
L4-YA
ns
*
**
***
F
0.2 µm
G
Distance (nm)
Between edges
Between centers

Figure 1

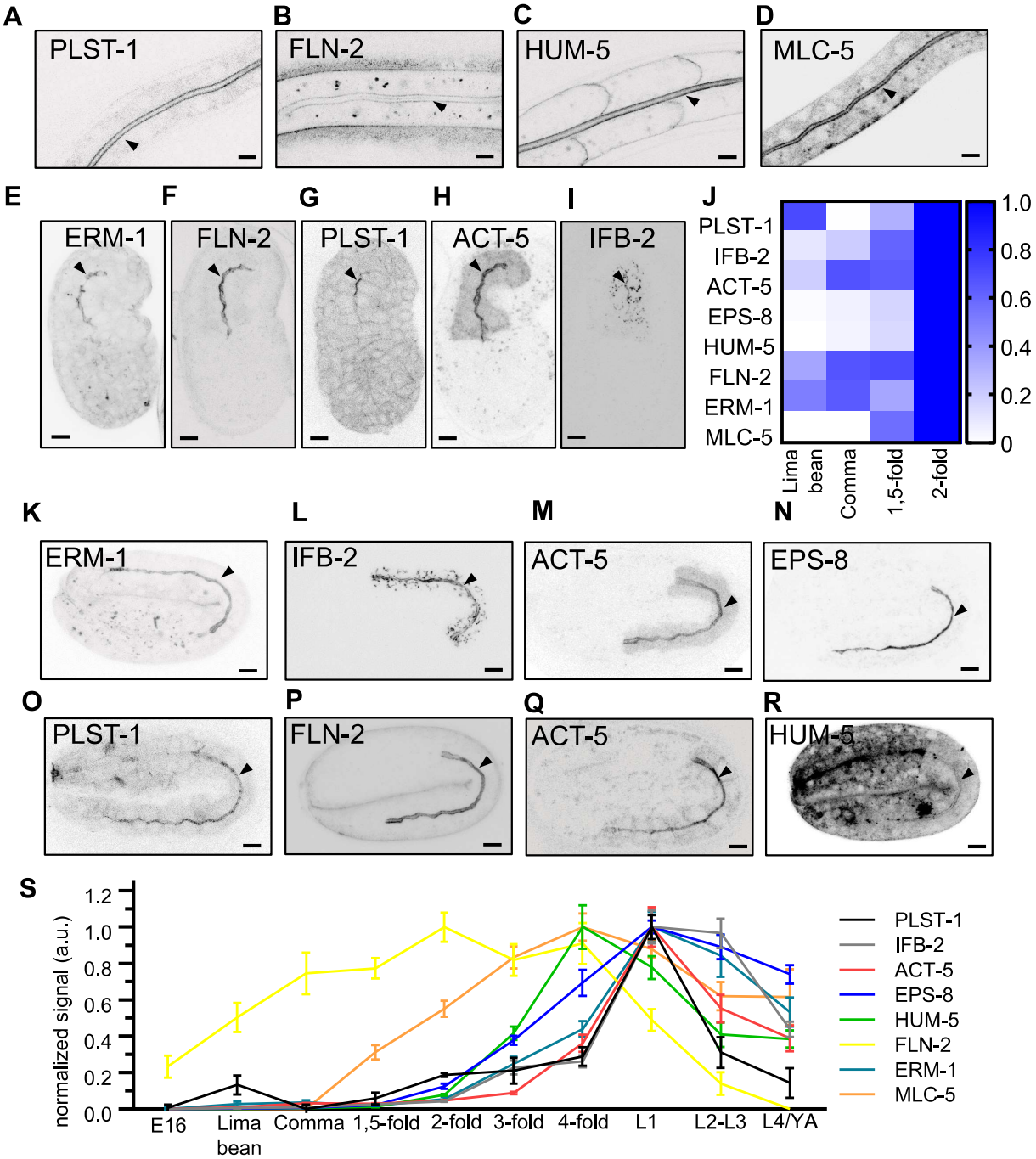
A
PLST-1
B
FLN-2
C
HUM-5
D
MLC-5
E
ERM-1
F
FLN-2
G
PLST-1
H
ACT-5
I
IFB-2
J
PLST-1
IFB-2
ACT-5
EPS-8
HUM-5
FLN-2
ERM-1
MLC-5
Lima bean
Comma
1,5-fold
2-fold
1.0
0.8
0.6
0.4
0.2
0
K
ERM-1
L
IFB-2
M
ACT-5
N
EPS-8
O
PLST-1
P
FLN-2
Q
ACT-5
R
HUM-5
S
normalized signal (a.u.)
1.2
1.0
0.8
0.6
0.4
0.2
0.0
E16
Lima bean
Comma
1,5-fold
2-fold
3-fold
4-fold
L1
L2-L3
L4/YA
PLST-1
IFB-2
ACT-5
EPS-8
HUM-5
FLN-2
ERM-1
MLC-5

Figure 2

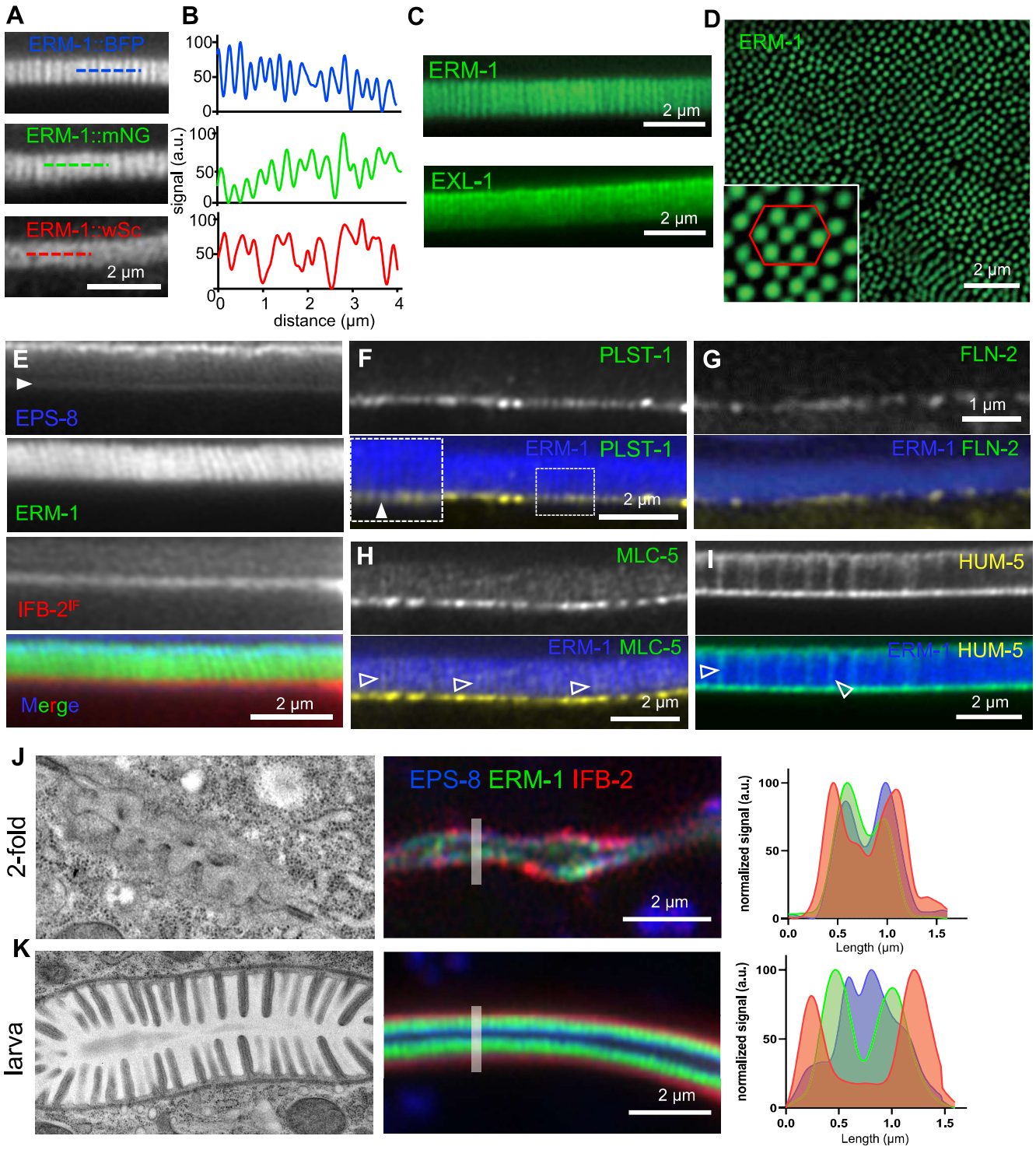
A
ERM-1::BFP
ERM-1::mNG
ERM-1::wSc
2 µm
B
signal (a.u.)
distance (µm)
C
ERM-1
EXL-1
2 µm
D
ERM-1
2 µm
E
EPS-8
ERM-1
IFB-2IF
Merge
2 µm
F
PLST-1
ERM-1 PLST-1
2 µm
G
FLN-2
1 µm
ERM-1 FLN-2
H
MLC-5
ERM-1 MLC-5
2 µm
I
HUM-5
ERM-1 HUM-5
2 µm
J
2-fold
EPS-8 ERM-1 IFB-2
2 µm
normalized signal (a.u.)
Length (µm)
K
larva
2 µm
normalized signal (a.u.)
Length (µm)

Figure 3

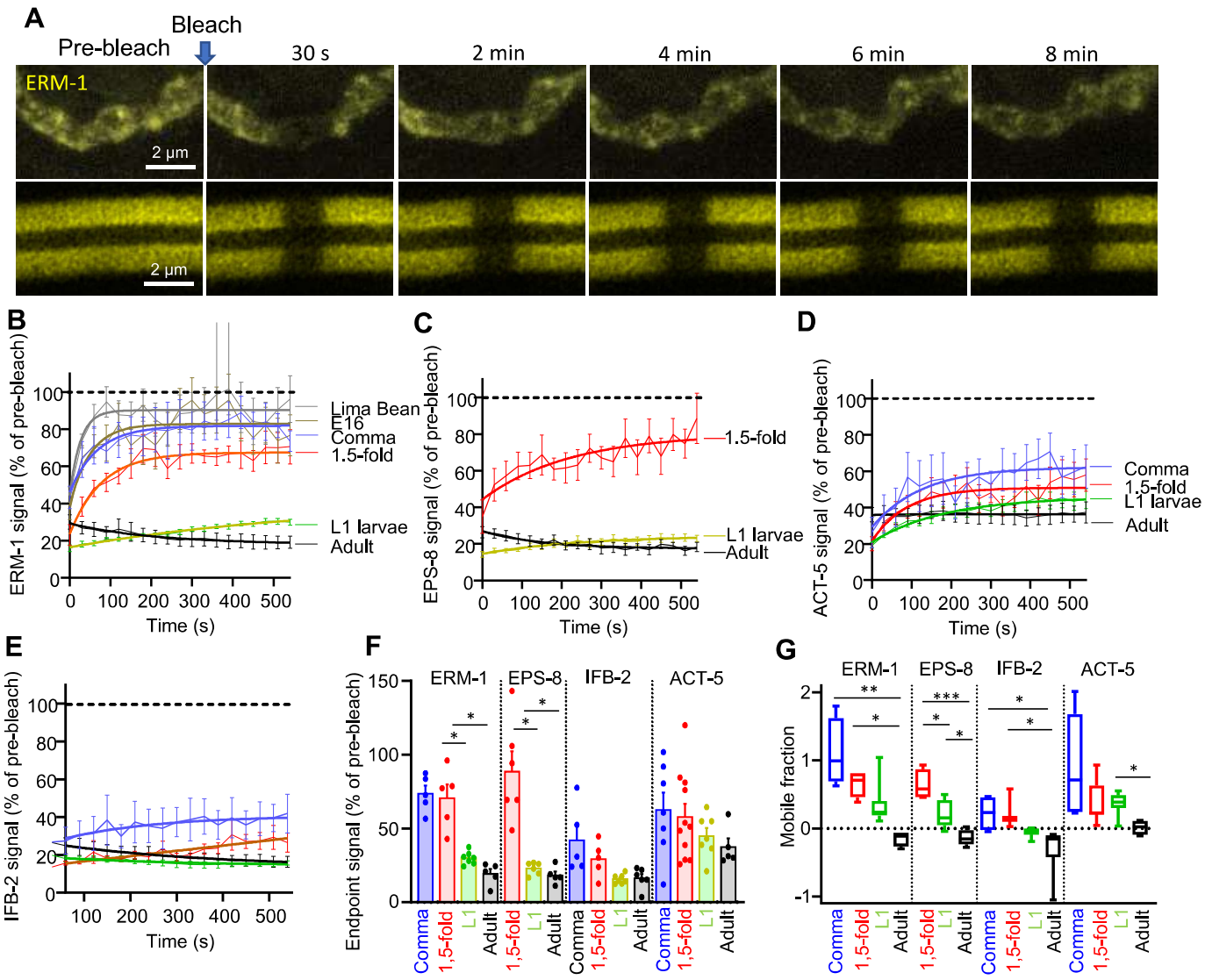
A
Pre-bleach
Bleach
30 s
2 min
4 min
6 min
8 min
ERM-1
2 µm
2 µm
B
ERM-1 signal (% of pre-bleach)
Time (s)
Lima Bean
E16
Comma
1.5-fold
L1 larvae
Adult
C
EPS-8 signal (% of pre-bleach)
Time (s)
1.5-fold
L1 larvae
Adult
D
ACT-5 signal (% of pre-bleach)
Time (s)
Comma
1.5-fold
L1 larvae
Adult
E
IFB-2 signal (% of pre-bleach)
Time (s)
F
Endpoint signal (% of pre-bleach)
ERM-1
EPS-8
IFB-2
ACT-5
Comma
1,5-fold
L1
Adult
G
Mobile fraction
ERM-1
EPS-8
IFB-2
ACT-5
Comma
1,5-fold
L1
Adult

Figure 4

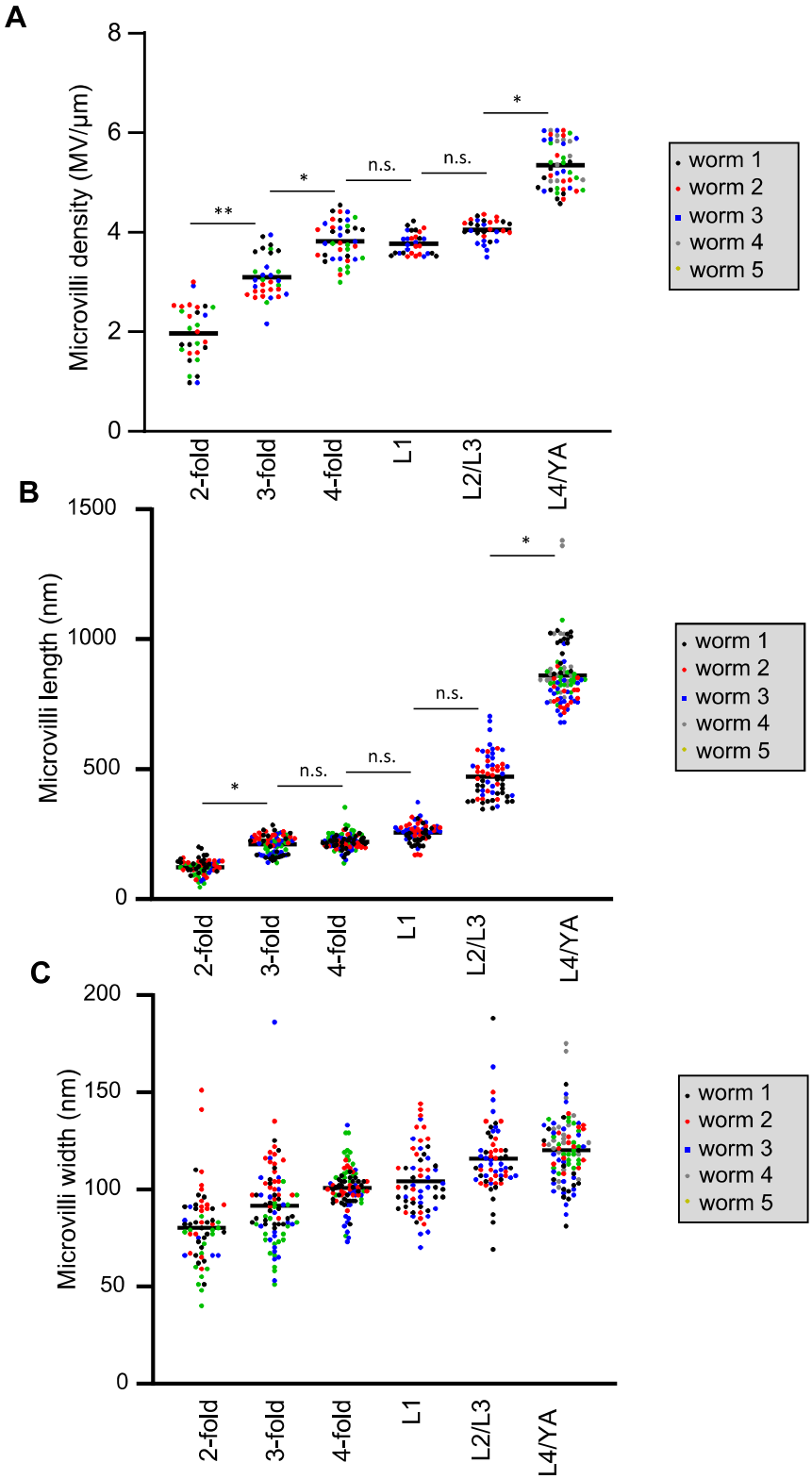

Figure S1. Individual values of brush border measurements by TEM, related to Fig. 1.
Colorized dots represent individual worms at the indicated developmental stages. Bar is the grand mean of all the measurements. Microvilli density was measured on 3-13 slices/worm, microvilli length and width on 6-29 microvilli/worm. N.s., non-significant, *p<0,05, **p<0,01, Mann-Whitney test (A-B) and unpaired t-test (C).

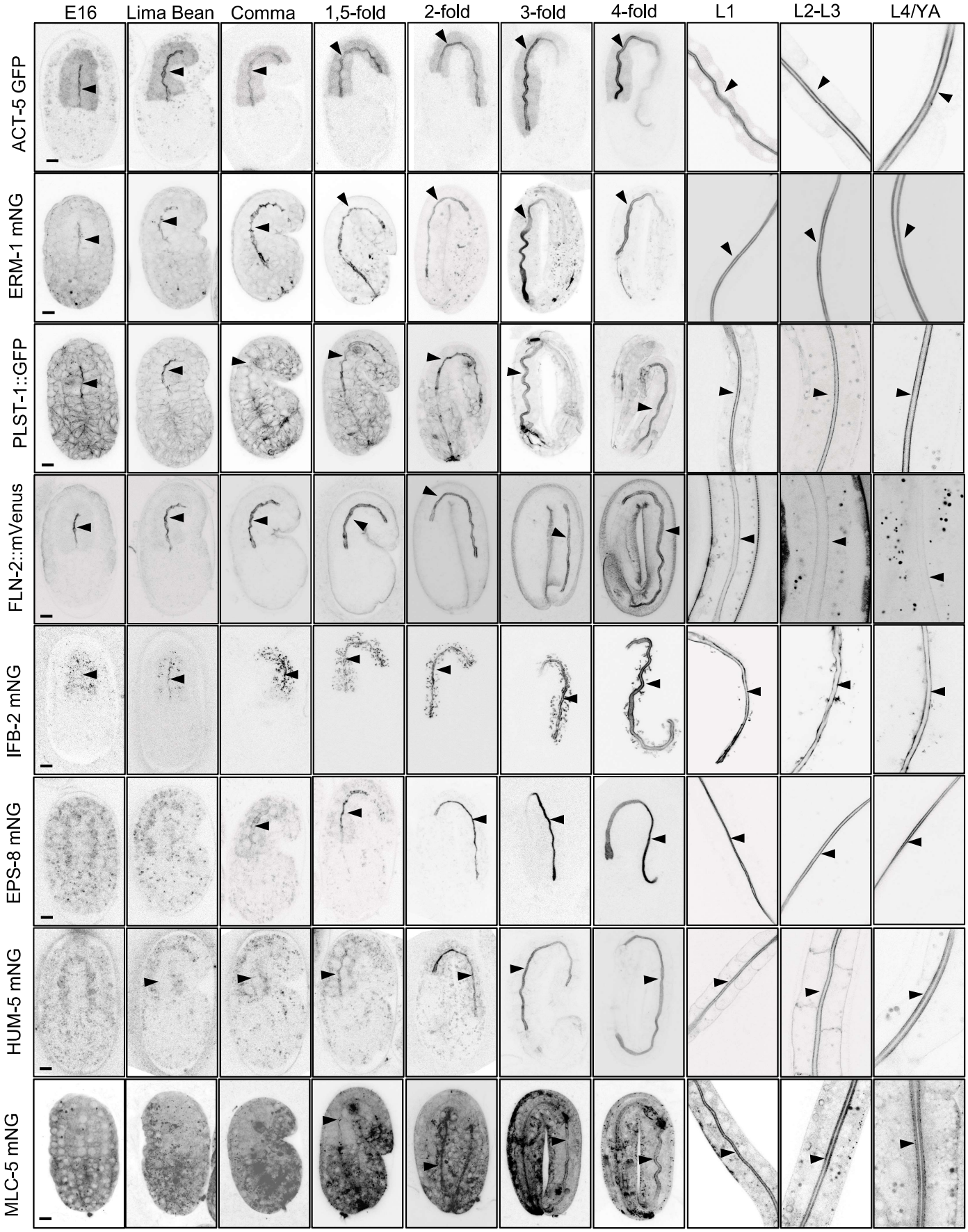

Figure S2. Systematic analysis of brush border markers during *C. elegans* development. Representative confocal images of the endogenously tagged markers indicated (except ACT-5::GFP). Arrowheads show the intestinal cells apical PM. Scale bar is 5 μm.

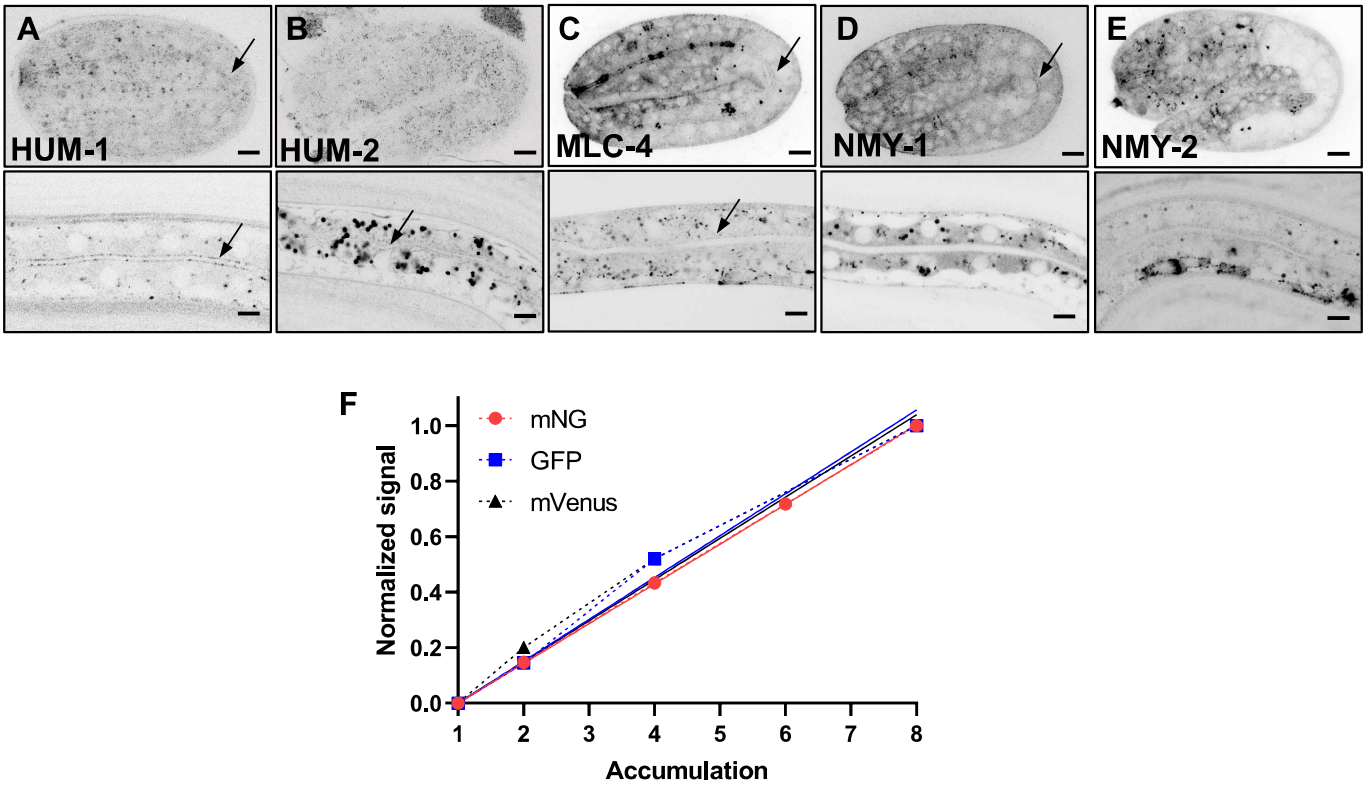

Figure S3. Systematic analysis of brush border markers during *C. elegans* development.
(A-E) Representative confocal images of *C. elegans* strains expressing endogenously tagged versions of the indicated markers, which showed no apical accumulation during *C. elegans* intestine development. (F) Control of the quantitative assessment of brush border markers arrival at the apical PM. Accumulation of ERM-1::mNG, PLST-1::GFP and FLN-2::mVenus signal linearly increases with image accumulation. Scale bar, 5 μm.

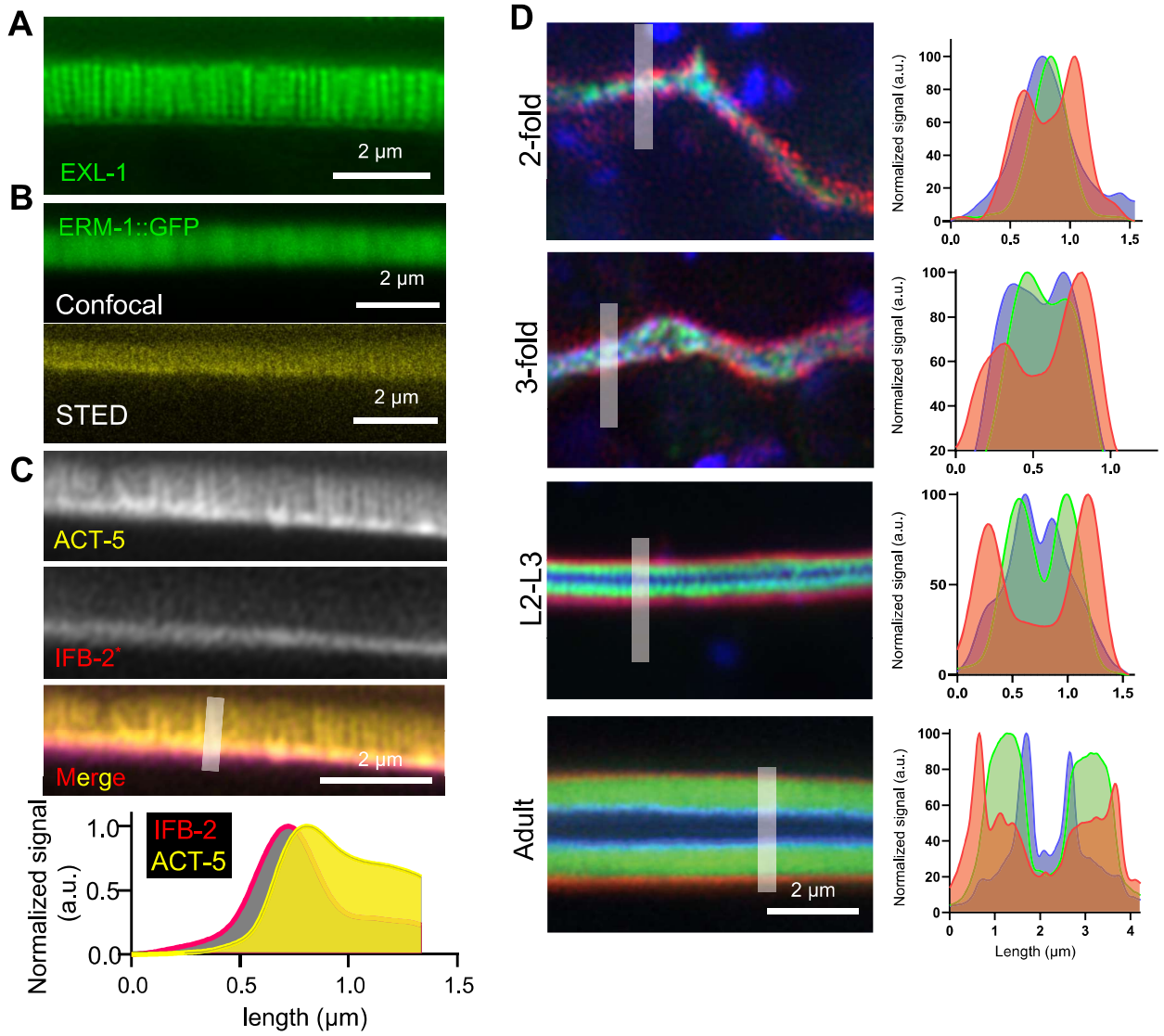

Figure S4. Super-resolution imaging of brush border markers *in vivo*. (A) Representative super-resolution image of exogenously expressed EXL-1::GFP. (B) ERM-1::GFP was imaged in adult worms using the indicated microscopes. (C) Super-resolution images of a *C. elegans* adults co-expressing ACT-5::GFP and IFB-2::wSc. Bottom panel shows a normalized intensity profile along the line depicted in grey. (D) Representative images of the localization of endogenously tagged EPS-8::BFP, ERM-1::mNG and IFB-2::wSc in *C. elegans* at the indicated developmental stages. Right panels show an intensity profile of the three markers along the line depicted in left panels. Scale bars, 2 µm.

.

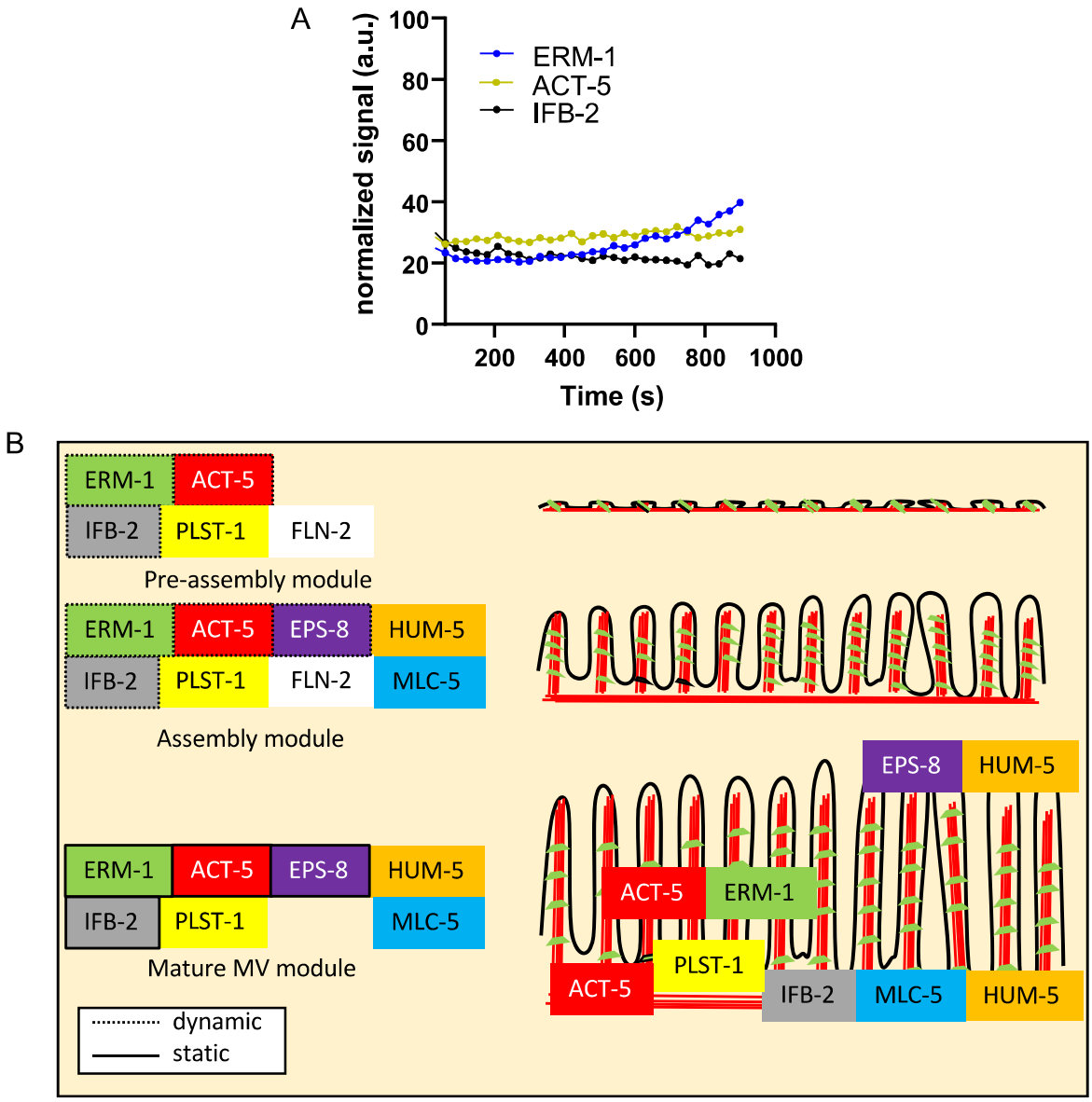

Figure S5. Dynamic recruitment of brush border components.
(A) Longer measurement of brush border components dynamics in adult worms. The curves show the recovery of ERM-1::mNG, IFB-2::mNG and ACT-5::GFP signal every 30 s after photobleaching, measured for an extended time, n=1 for each marker. (B) Model of brush border assembly *in vivo* in *C. elegans*. Microvilli are built from a preformed *pre-assembly module* and grow through the dynamic recruitment of brush border components, which become highly stable in the mature brush border.

Strain	Markers	Genotype	Reference
FBR 96	MLC-4	mlc-4(jme04[mlc-4::eGFP+loxP])III	Francois Robin lab
FBR140	MLC-5	mlc-5(jme09[GFP^3xFLAG::mlc-5])III	Francois Robin lab
FBR222	FLN-2	fln-2(jme-19[fln-2::mVenus]) X	Francois Robin lab
FL274	ERM-1, IFB-2	erm-1(bab59[erm-1::mNG^SEC^3xFlag]) I ; ifb-2(bab142[ifb-2::wSc]) II	Bidaud-Meynard et al., Development, 2019
FL290	EPS-8	eps-8(bab140[eps-8::mNG]) IV	This study
FL378	ERM-1	erm-1(bab59[erm-1::mNG^3xFlag]) I	Bidaud-Meynard et al., Development, 2019
FL379	ERM-1	bab64[erm-1::wrmSc^3xFlag] I	Bidaud-Meynard et al., Development, 2019
FL381	ACT-5, IFB-2	fgEx12 (act-5p::act-5::gfp); ifb-2(bab142[ifb-2::wrmSc]) II	This study
FL383	EPS-8, ERM-1, IFB-2	eps-8(bab140[eps-8::mNG]) IV ; erm-1(bab59[erm-1::mNG^SEC^3xFlag]) I; IFB-2	This study
FL384	ERM-1	erm-1(bab167[erm-1::degron-tagBFP2])	This study
FL385	IFB-2	ifb-2(bab153[ifb-2::mNG]) II	This study
FL386	ERM-1, PLST1	erm-1(bab167[erm-1::degron-tagBFP2]) ; plst-1(msn190[plst-1::gfp]) IV	This study
FL387	ERM1, HUM5	erm-1(bab167[erm-1::degron-tagBFP2]) ; hum-5(bab189[hum-5::mNG])	This study
FL388	ERM-1, MLC5	erm-1(bab167[erm-1::degron-tagBFP2]) ; mlc-5(jme09[GFP^3xFLAG::mlc-5])III	This study
FL586	ERM-1, FLN-2	erm-1(bab167[erm-1::degron-tagBFP2])	This study
LP162	NMY-2	nmy-2(cp13[nmy-2::GFP + LoxP]) I	CGC
LP462	MRCK-1	mrck-1(cp189[mrck-1::GFP::3xFlag]) V	CGC
MCP111	PGP-1	pgp-1(bab111[mNG^3xFlag::pgp-1]) IV	Bidaud-Meynard et al., Development, 2019
MCP184	HUM-2	hum-2(bab184[hum-2::mNG])	This study
MCP189	HUM-5	hum-5(bab189[hum-5::mNG])	This study
MCP223	EXL-1	exl-1(bab223[exl-1::mNG])	This study
ML2540	NMY-1	nmy-1(mc82[nmy-1::gfp]) X.	Vuong-Brender TTK, et al. eLife 2017
OH2211	EXL-1	otEx1184 [exl-1p::exl-1::GFP + rol-6(su1006)]	CGC
QQ226	HUM-1	hum-1(cv21[hum-1::RFP]) I	CGC
RZB213	PLST-1	plst-1 (msn190[plst-1::gfp]) IV	Ding WY et al J Cell Biol 2017
VJ268	ACT-5	fgEx12 (act-5p::act-5::gfp)	Zhang et al., 2012

Table S1. *C. elegans* strains used in this study.